Master Laboratory

Compton Scattering

Group

Performed on April 12th–April 16th
under supervision of

Abstract

The Compton effect describes the scattering of photons with free electrons at rest. In this experiment we investigate Compton scattering and in particular the conservation of energy in the scattering as well as the differential cross section both with respect to varying scattering angles.

The spectra of two radioactive sources, ^{22}Na and ^{137}Cs were recorded using a sodium iodide and a plastic scintillator attached to a NIM electronics set-up. By fitting photo peak and Compton edges both scintillators were calibrated. Installing the plastic scintillator between the ^{137}Cs source and the NaI scintillator reduces the intensity by 5 %.

With a coincidence-setup, Compton-scattering specific events could be reconstructed. This way, the energy conservation during Compton scattering could be confirmed. Further, the differential cross section was calculated for various angles and the overall trend of the differential cross section as described by the Klein-Nishina formula could be confirmed with a residual standard error of $\chi^2/\mathrm{df} = 1.2$.

Contents

1. Introduction

The interaction of light with matter one can discern three main phenomenons: the photo effect, Compton scattering and pair production. This report and the experiment presented in it focuses on and studies the phenomenon of Compton scattering.

Arthur Holly Compton observed a shift in the wavelength of photons when scattered at quasi free electrons in 1923. Nowadays this observation is called the Compton effect and the process Compton scattering in honoring of Arthur Compton [3].

The goal of the experiment presented in the paper was to measure Compton scattering and studying the expected conservation of energy as well as the cross section of Compton scattering. This is done by using two different scintillator in coincidence mode. For one, a plastic scintillator is used as a target for the Compton scattering and to measure the energy of the scattered electrons and furthermore a inorganic (NaI) scintillator is used to measure the scattered electrons. The source used to get initial photons is ^{137}Cs which emits photons with 662 keV.

The report is structured as follows: hereafter, in section 2 the theoretical basics needed to follow the experiment and its analysis are briefly described. Afterwards in section 3 we explain the setup used in the experiment and how the experiment was carried out. This is followed by a presentation of the analysis done with the measured data in section 4. In section 5 the results obtained in the analysis are summarized and discussed.

2. Theory

2.1. Interactions of light with matter

Photoelectric effect The phenomenon that an incoming photon strikes a bound electron out of an atomic shell is called the photoelectric effect [8]. After absorption of the incident photon with energy E_γ, an electron with the initial-state binding energy E_b obtains the kinetic energy

$$T_e' = E_\gamma - E_\mathrm{b}. \tag{1}$$

Electrons of this type are often referred to as photoelectrons. The photon-electron interaction leaves a vacancy in one of the atomic shells which is immediately filled by an electron in a higher shell. During that process, a photon of a distinct wavelength (usually in the form of X-ray radiation) is emitted which, in turn, can produce more photoelectrons in the detector material. As the total energy of these is eventually transferred to the optical scintillation photons, the energy peak measured due to the photoelectric effect is extremely sharp, provided the incident photon's energy is well-defined. The typical energy scale of the photoelectric effect is in the lower keV range [7].

Due to conservation of energy and momentum, the photoelectric effect only affects bound electrons as the atomic nucleus absorbs some recoil energy. The total cross section of the photoelectric effect is proportional to $Z^5/E_\gamma^{3.5}$, where Z is the proton number of the atom, presupposed that the photons energy is small compared to the electron mass [7], i. e. $E_\gamma \ll m_e c^2$.

Compton effect One of the possibilities of light interacting with matter is by the Compton effect (also known as Compton scattering): In the course of this, a photon collides elastically with a free electron that is initially assumed to be at rest. The incident photon transfers some of its energy to the electron in the form of kinetic energy, thereby reducing its wavelength. In the following we will describe this effect quantitatively.

Suppose that the photon has an initial energy E_γ, frequency f and relativistic momentum $\boldsymbol{p}_\gamma$, while the electrons initial energy and momentum will be denoted E_e and $\boldsymbol{p}_e$, respectively. Further, the corresponding quantities after the scattering will be denoted by a prime ($'$). By conservation of energy and momentum, we have

$$E_\gamma + E_e = E_\gamma' + E_e', \tag{2}$$

$$\boldsymbol{p}_\gamma = \boldsymbol{p}_\gamma' + \boldsymbol{p}_e', \tag{3}$$

where the assumption that the electron was at rest initially imposed $\boldsymbol{p}_e = 0$. This further implies that the electron's initial energy is given by $E_e = m_e c^2$, where m_e refers to its rest mass. By the relativistic energy-momentum relation, the electron's energy in the final state is given by $E_e' = \sqrt{(\boldsymbol{p}_e' c)^2 + (m_e c^2)^2}$, while the photon's energies are given by the Planck-Einstein relations as $E_\gamma = hf, E_\gamma' = hf'$. Inserting these relations into

eq. (2) gives

$$hf + m_e c^2 = hf' + \sqrt{(\boldsymbol{p}'_e c)^2 + (m_e c^2)^2} \tag{4}$$

$$\iff \quad (\boldsymbol{p}'_e c)^2 = (hf - hf' + m_e c^2)^2 - (m_e c^2)^2. \tag{5}$$

Now, note that eq. (3) can be rearranged to be inserted in the left-hand side of the equation above:

$$\begin{aligned}(\boldsymbol{p}'_e c)^2 &= c^2(\boldsymbol{p}'_e \cdot \boldsymbol{p}'_e) \\ &= c^2(\boldsymbol{p}_\gamma - \boldsymbol{p}'_\gamma) \cdot (\boldsymbol{p}_\gamma - \boldsymbol{p}'_\gamma) \\ &= c^2\left[\boldsymbol{p}_\gamma^2 + (\boldsymbol{p}'_\gamma)^2 - 2|\boldsymbol{p}_\gamma||\boldsymbol{p}'_\gamma|\cos\vartheta\right] \\ &= (hf)^2 + (hf')^2 - 2h^2 ff'\cos\vartheta,\end{aligned} \tag{6}$$

where ϑ refers to the angle between the incoming and outgoing photon (cf. fig. 1 for the underlying geometry). Equating the equation above with the right-hand side of eq. (5) then gives

$$\begin{aligned}(hf)^2 + (hf')^2 - 2h^2 ff'\cos\vartheta &= \left(h(f-f')^2 - hf' + m_e c^2\right)^2 - (m_e c^2)^2 \\ \iff \quad f^2 + (f')^2 - 2ff'\cos\vartheta &= (f-f')^2 + \frac{2m_e c^2}{h}(f-f') \\ \iff \quad -2ff'\cos\vartheta &= -2ff' + \frac{2m_e c^2}{h}(f-f') \\ \iff \quad f - f' &= \frac{h}{m_e c^2} ff'(1-\cos\vartheta).\end{aligned} \tag{7}$$

The formula may now be multiplied by $c/(ff')$ to yield the difference in the photon's wavelength by using $\lambda = c/f$:

$$\frac{c}{f'} - \frac{c}{f} = \lambda' - \lambda = \frac{h}{m_e c}(1-\cos\vartheta). \tag{8}$$

Equation (8) describes the total shift in wavelength of the photon due to Compton scattering. Note that the right-hand side is non-negative, implying that the wavelength in the final state will always be longer than that of the initial state. If we are interested in the energy balance we may use the Planck-Einstein relation again and rearrange eq. (8) for f':

$$\begin{aligned}E'_\gamma = hf' &= h \cdot \frac{1}{\frac{h}{m_e c^2}(1-\cos\vartheta) + \frac{1}{f}} \\ &= \frac{hf}{1 + \frac{hf}{m_e c^2}(1-\cos\vartheta)} = \frac{E_\gamma}{1 + \frac{E_\gamma}{m_e c^2}(1-\cos\vartheta)}.\end{aligned} \tag{9}$$

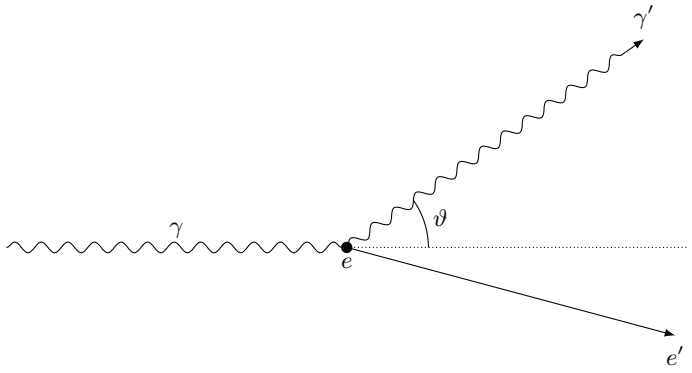

Figure 1: Geometry of the Compton interaction.

From this, the energy transfer ΔE from the photon to the electron is readily calculated:

$$\begin{aligned}\Delta E &= E_\gamma - E'_\gamma \\ &= E_\gamma \left(1 - \frac{1}{1 + \frac{E_\gamma}{m_e c^2}(1 - \cos\vartheta)}\right) \\ &= E_\gamma \frac{\frac{E_\gamma}{m_e c^2}(1 - \cos\vartheta)}{1 + \frac{E_\gamma}{m_e c^2}(1 - \cos\vartheta)}.\end{aligned} \tag{10}$$

As the electron is at rest initially, the energy transfer ΔE corresponds to the kinetic energy of the final-state electron. While the energy transfer approaches zero as $\vartheta \to 0$, there exists a maximum at $\vartheta = \pi$ as is easily checked. The maximum kinetic energy of the electron for a given initial energy E_γ of the photon is thus

$$\Delta E_{\max} = E_\gamma \frac{2\frac{E_\gamma}{m_e c^2}}{1 + \frac{E_\gamma}{m_e c^2}} = \frac{E_\gamma}{1 + \frac{m_e c^2}{2E_\gamma}}. \tag{11}$$

Due to a maximum energy transfer existing, the theoretical energy distribution of an electron scattered via Compton distribution has a sharp cutoff which is known as the Compton edge. As we rely on the Compton edge's location on calibrating the channels of the multi-channel analyzer in pulse-height analysis mode, it is useful to give an analytic model of the compton edge. Then, the parameters of the analytical model can be used for analyzing the exact location of the compton edge. A very simple model for an ideal compton edge is given by a second-order polynomial which gets cut off below the compton edge [9]: If N is the counting rate with respect to energy of the model, we have

$$N(E) = \begin{cases} aE^2 + bE + c & \text{if } E \leq E_{\mathrm{C}}, \\ 0 & \text{if } E > E_{\mathrm{C}}, \end{cases} \tag{12}$$

ideally, where E_{C} refers to the exact location of the Compton edge. The main idea is that the real counting rate is given as a convolution of the ideal counting rate with a

centered Gaussian distribution

$$G_{0,\sigma}(E) = \frac{1}{\sqrt{2\pi\sigma^2}} \exp\left(-\frac{E^2}{2\sigma^2}\right). \tag{13}$$

The convolution is readily calculated to be

$$\begin{aligned}(r * G_{0,\sigma})(E) = &\int_{-\infty}^{\infty} N(x) G_{0,\sigma}(E - X)\,\mathrm{d}x \\ &= \frac{1}{2}\left[a(E^2+\sigma^2) + bE + c\right] \operatorname{erfc}\left(\frac{E - E_\mathrm{C}}{\sqrt{2}\sigma}\right) \\ &\quad - \left[b - \frac{\sigma}{\sqrt{2\pi}} a(E + E_\mathrm{C})\right] \exp\left(-\frac{(E-E_\mathrm{C})^2}{2\sigma^2}\right).\end{aligned} \tag{14}$$

Here, erfc refers to the complementary error function. By fitting eq. (14) to the observed counting rate with a, b, c, E_C, and σ as fit parameters, the location of the Compton edge is then given as E_C.

The differential cross section of Compton scattering is given in lowest order of quantum electrodynamics by the Klein-Nishina formula [7, rearranged]:

$$\frac{\mathrm{d}\sigma}{\mathrm{d}\Omega} = \frac{r_e^2}{2} \frac{1}{[1 + \frac{E_\gamma}{m_e c^2}(1 - \cos\vartheta)]^2} \left[\frac{1}{1 + \frac{E_\gamma}{m_e c^2}(1-\cos\vartheta)} + 1 + \frac{E_\gamma}{m_e c^2}(1 - \cos\vartheta) - \sin^2\vartheta\right]. \tag{15}$$

The Klein-Nishina formula can also be expressed in terms of the energies of the photon before and after the scattering:

$$\frac{\mathrm{d}\sigma}{\mathrm{d}\Omega} = \frac{r_e^2}{2} \frac{E_\gamma^2}{{E'_\gamma}^2} [\frac{E_\gamma}{E'_\gamma} + \frac{E'_\gamma}{E_\gamma} - \sin^2\vartheta] \tag{16}$$

Here, $r_e = \frac{1}{4\pi\varepsilon_0}\frac{e^2}{m_e c^2} \approx 2.818 \times 10^{-15}\,\mathrm{m}$ refers to the classical electron radius. Note that for $E_\gamma = 0$, the Klein-Nishina formula reduces to the differential cross section for Thomson scattering [7],

$$\frac{\mathrm{d}\sigma}{\mathrm{d}\Omega} = \frac{r_e^2}{2}(1 + \cos^2\vartheta). \tag{17}$$

Thomson scattering itself describes the scattering of an electromagnetic wave on free electrons within the scope of classical electromagnetism: The free electrons are excited by the external oscillating field and emit dipole radiation of the same wavelength of the incoming wave, that is, the wavelength is not shifted.

Both the differential cross section of Thomson scattering and Compton scattering as predicted by the Klein-Nishina formula is sketched in fig. 2 as a function of the scattering angle.

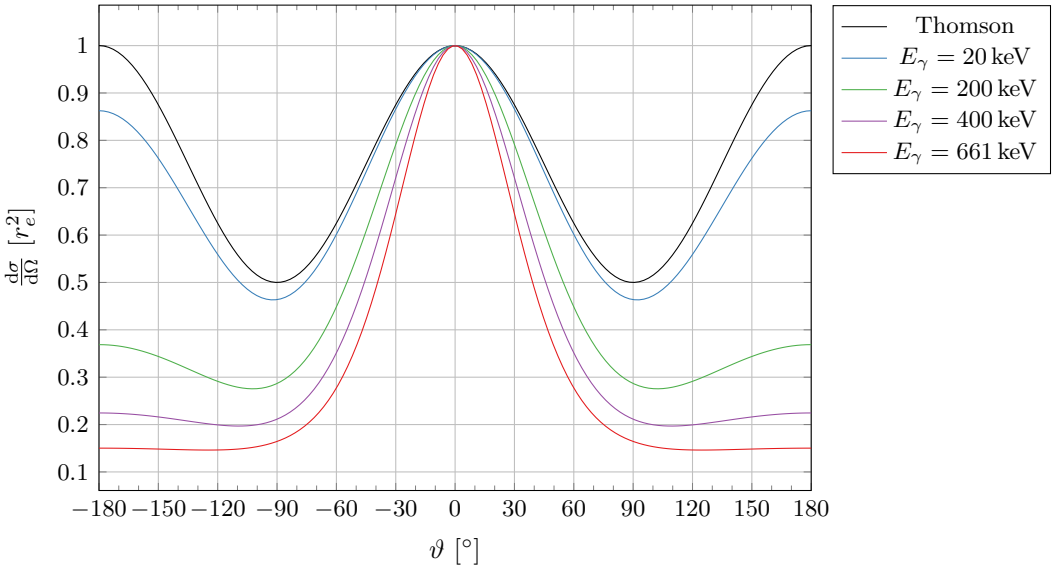

Figure 2: Differential cross section of Thomson scattering and for Compton scattering (with the Klein-Nishina formula); the latter for various photon energies. Note that the line corresponding to $E_\gamma = 661\,\mathrm{keV}$ is the one we wish to measure in the experiment.

Pair production Pair production describes the process of a photon being converted into an electron-positron pair and occurs mainly in the Coulomb field of a charged nucleus [7]. The photon's energy must exceed the sum of electron and positron mass as well as the recoil energy to the atomic nucleus (although the latter is negligible for most nuclei). Therefore, for pair production to occur, we require $E_\gamma > 2m_e c^2$. As positrons are anti-particles, the positron's lifetime is limited in the detector material, annihilating with another electron to Positronium which is itself highly unstable and decays within $10^{-7}\,\mathrm{s}$ to $10^{-9}\,\mathrm{s}$ under emission of several photons (in most cases two). Both photons now carry an energy of about the rest mass of an electron/positron by energy conservation. Due to conservation of momentum, the angle between the photons emitted in this manner amounts to 180°. There are now several possibilities these photons manifest themselves as detector signals [8]: One possibility is that neither of the photons escape and interact with the detector material via Compton scattering or Photo effect, adding to the photo peak. Another possibility is that one of the photons escapes, while the remaining photon can be registered as single-escape peak at $\approx E_\gamma - m_e c^2$. A third option is that both photons escape, which will be registered as a double-escape peak at $\approx E_\gamma - 2m_e c^2$.

2.2. Devices used in the experiment

In the following, the functional principle of some of the devices used in the experiment is explained briefly.

2.2.1. Scintillation counter

A scintillation counter usually consists of a scintillator and a photomultiplier. Scintillators in turn consist of organic or inorganic materials that emit multiple light photons when exposed to electromagnetic radiation. This light is then absorbed by a photomultiplier which is then responsible for producing an electric signal that can be analyzed using NIM electronics, for example.

Inorganic scintillators Most inorganic scintillators are crystals that show luminescent properties. The inorganic scintillator that we use in our experiment is a sodium iodide (NaI) crystal that is doped with Thallium (Ti). The working principle of this scintillator is best explained by considering the valence and conduction bands of the material: If a photon hits an electron in the valence band, the electron obtains enough energy to transfer to the conduction band, leaving behind a vacancy. In the case of an un-doped sodium iodide crystal, the electron would simply fall back to that vacancy, emitting a photon of the same energy as the incidence photon and the process repeats. However, in the case of Thallium doped sodium iodide, the conduction band is locally deformed in a way that the energy level in the conduction band is lower near the activator atoms. Now, if an excited electron fills the vacancy it created prior, the photon emitted in the process has a lower energy than the photon in the un-doped case such that it can now longer excite other electrons. Thus, the photon is no longer absorbed by the crystal and can travel to the photo cathode of the photomultiplier.

Inorganic scintillators are preferred when one is interested in a great energy resolution over time resolution, as inorganic scintillators have a much higher cooldown than organic scintillators.

Organic scintillators The second scintillator we use is a plastic scintillator. These is based on the excitation and de-excitation of organic molecular structures which form a transparent medium which is solid in our case (but can also be liquid) [7]. When radiation hits these molecules, they become excited and emit photons upon excitation. As with the inorganic scintillator, activators are also implanted which ensure that photons emitted by these molecules are not reabsorbed by the scintillator. Unlike the inorganic scintillator, the plastic scintillator requires a very high activation energy and has a lower light yield.

The plastic scintillator is used for two main reasons: Firstly, the Compton scattering happens within the plastic scintillator as the scattered electrons have a small coverage. Secondly, the plastic scintillator comes with a very precise time resolution. As it mostly consists of organic material and thus of materials with low proton numbers, we won't expect a photon peak in the plastic scintillator's spectrum (cf. section 2.1). Further, due to the energy resolution being lower than the one of the sodium iodide scintillator, the Compton edge will be noisier.

Photomultiplier A photomultiplier is used to detect light signals and convert them into an electric signal that is proportional to the intensity of the incoming photons. The schematic structure of a photomultiplier is shown in fig. 3. Let's say that a photon

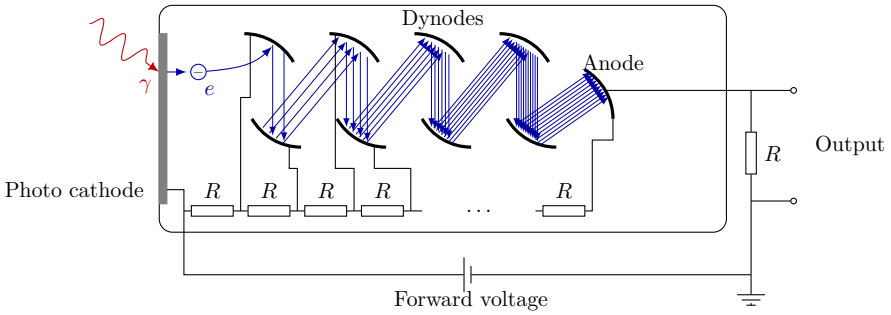

Figure 3: Schematic representation of the working principle of a photomultiplier.

emitted by a scintillator hits the photo cathode of the photomultiplier. Due to the photoelectric effect, a photo electron is knocked out of the cathode and travels to the inside of the photomultiplier. There, it is subject to the electric field generated by a series of dynodes. Each successive dynode features a higher electric potential than the one before it. The photo electron accelerates towards the first dynode where secondary electrons are ejected by the photoelectric effect. These electrons again travel to the next dynodes where they again knock out electrons and the cycle repeats. The resulting electron avalanche can be detected at the end of the photomultiplier. Under normal conditions, the output current of the photomultiplier is proportional to the number of incoming electrons [8]. This means that a photomultiplier can be used in conjunction with a scintillator to measure the energy of incoming photons.

2.2.2. NIM electronics

The output of the scintillation counters which are in close proximity to the radioactive sources is routed through a setup consisting of multiple NIM devices before a spectrum can be analyzed at the computer. The purpose of some NIM devices used in the experiment is briefly described below.

Preamplifier Closely attached to the photomultiplier is the preamplifier. The preamplifier's purpose is not only to amplify the photomultiplier's weak signal, but also to enhance the signal/noise ratio. To minimize the influence of stray fields, each preamplifier is directly attached to a photomultiplier.

Main amplifier The signal of the preamplifier is routed to the main amplifier. The main amplifier amplifies the signal and reduces an effect known as pile-up: when two signals arrive at roughly the same time it can happen that both signals add up, falsifying the signal's amplitude. The amplifier's output can either be uni- or bipolar: The unipolar output signal carries more information about the pulse's height while the bipolar signal is better used for timing purposes.

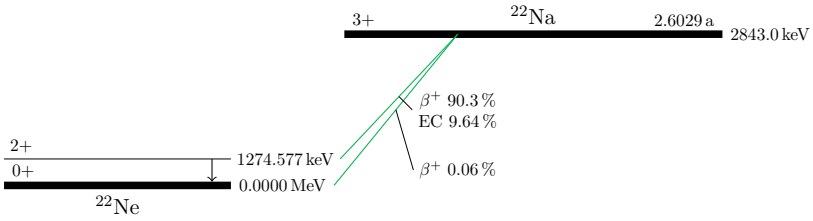

Figure 4: Decay scheme of ^{22}Na. Adapted from ref. [2].

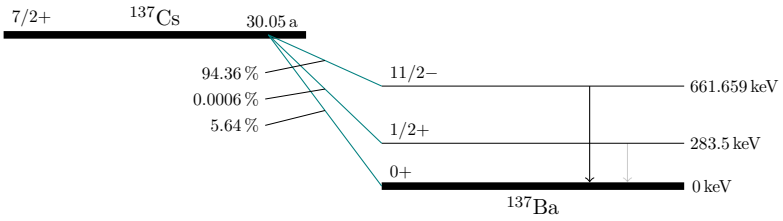

Figure 5: Decay scheme of ^{137}Cs. Adapted from ref. [1].

Timed single-channel analyzer The analog signals of the amplifier can be fed into a timed single-channel analyzer (TSCA). The TSCA generates logical signals based on the height of the input pulse: By setting values for a lower and an upper level, a logical signal is dispensed each time a signal is registered by the TSCA that is within lower and upper level. The output signal can be delayed by an additional delay knob.

Linear gate and coincidence unit The TSCA is best used in conjunction with a linear gate or a coincidence unit: These devices accept one (in the case of a gate) or more (in the case of the coincidence unit) logical inputs and let an analogue signal pass, if all logical inputs attached to the device send a signal at the same time. This is useful for selecting events where multiple highly-correlated particles are measured at different scintillators. The coincidence unit can also be connected to a Hex-Scaler which counts simultaneous events in a pre-set time frame.

Multi-channel analyzer The multi-channel analyzer (MCA) – when operated in pulse-height analysis mode – accepts analogue inputs and orders them according to their pulse height into channels. A histogram of these event channels can be seen with the software "Gamma Acquisition & Analysis" which is run on the computer attached to the MCA. Further, the histogram may be exported in a digital file format.

2.3. Radioactive Preparations

In the following, the radioactive substances used and their main decays are briefly listed. The information was taken from the Table of Radionucldes [1, 2].

As for the radioactive substances, we use a ^{22}Na and a ^{137}Cs preparation. The main decays of ^{22}Na are sketched in fig. 4. The most probable decays are the decay via

electron capture and via β^+-decay to an excited state of ^{22}Ne. The decay scheme is sketched in fig. 4. As the excited state decays, a 1274.58 keV photon is emitted. If the decay happens via the β^+-decay, the resulting positron has an energy of 546.44 keV. The positron annihilates with a surrounding electron to form Positronium which decays under the emission of two 511 keV photons. For both the 1274.58 keV and the 511 keV we can calculate the location of the Compton edge by use of eq. (11):

$$\Delta E_{\max}(1274.58\,\text{keV}) = 1061.74\,\text{keV}, \tag{18}$$

$$\Delta E_{\max}(511\,\text{keV}) = 340.67\,\text{keV}. \tag{19}$$

As for the ^{137}Cs preparation, there are two major β^--decays. The less prominent of these is a direct decay into the ground state of ^{137}Ba, while the other is a decay into the 661.66 keV isomeric level of ^{137}Ba. The de-excitation releases a photon with that energy. Its Compton edge is located at

$$\Delta E_{\max}(661.66\,\text{keV}) = 477.336\,\text{keV} \tag{20}$$

which was again calculated by the use of eq. (11). The decay scheme of ^{137}Cs is sketched in fig. 5.

3. Setup and Procedure

3.1. Setup

The main components of this experiment are the radioactive sources already described in section 2.3 and two scintillators of different types, a Sodium Iodide (NaI) scintillator doped with Thallium as well as a plastic scintillator. As we want the Compton scattering to occur within the plastic scintillator, the tubular scintillation device is mounted in the middle of a circular metal plate. The NaI scintillator can then be fixed to the edge of the metal plate with a fixed angle engraved on that same plate.

The different radioactive sources are used at different parts of the experiment: The ^{22}Na source consists of a cylinder the size of a smaller pen and is only used for the energy calibration of both scintillators. As such it can be loosely placed between the two scintillators. The ^{137}Cs source, however, is used not only for energy calibration, but also the main parts of the experiment, investigating the energy conservation as well as the Klein-Nishina formula during Compton scattering. As the angle is of importance here, the considerably larger lead frame the source is enclosed in can be attached to the metal plate at a fixed angle.

Apart from the radiactive sources and the scintillators, the setup also consists of multiple NIM devices. An overview over the plugging diagram is shown in fig. 6. Both the plastic and the NaI scintillator and their photomultipliers are attached to preamplifiers which connect to main amplifiers. The main amplifier feature both unipolar and bipolar outputs. As mentioned in section 2.2, the bipolar signals have a better time resolution while the unipolar signals feature a richer energy resolution. The bipolar signals of both main amplifiers are thusly connected to the timing single channel analyzers (TSCA) on which the energy windows can be adjusted. The logical signals of both TSCAs end up in the coincidence unit along with the unipolar signal of the main amplifier from the plastic scintillator that is further delayed using a delay unit. The coincidence unit's purpose is to only let the unipolar signal of the plastic scintillator pass if there are logical signals from both TSCAs. As the coincidence unit has only one such gate function, a logical signal from the coincidence unit is also directed to a linear gate which regulates the (delayed) unipolar signal from the NaI scintillator. The output from the gate of both the coincidence unit and the linear gate are then routed each into a multi-channel analyzer (MCA).

For quick and rough measurements, the unipolar output of the coincidence unit can also be fed into a TSCA and then into a HEX counter which can count pulses within a specific time frame. This was mainly done to roughly quantify coincidences to refine the settings of the TSCAs.

3.2. Procedure

We started by preparing the setup to be ready for measuring coincidences by first placing the ^{22}Na source in between both scintillators and connecting the NIM electronics according to fig. 6. The primary goal now was to set the amplification levels of the main amplifiers such that all the channels of the MCAs were in use – too low an amplification

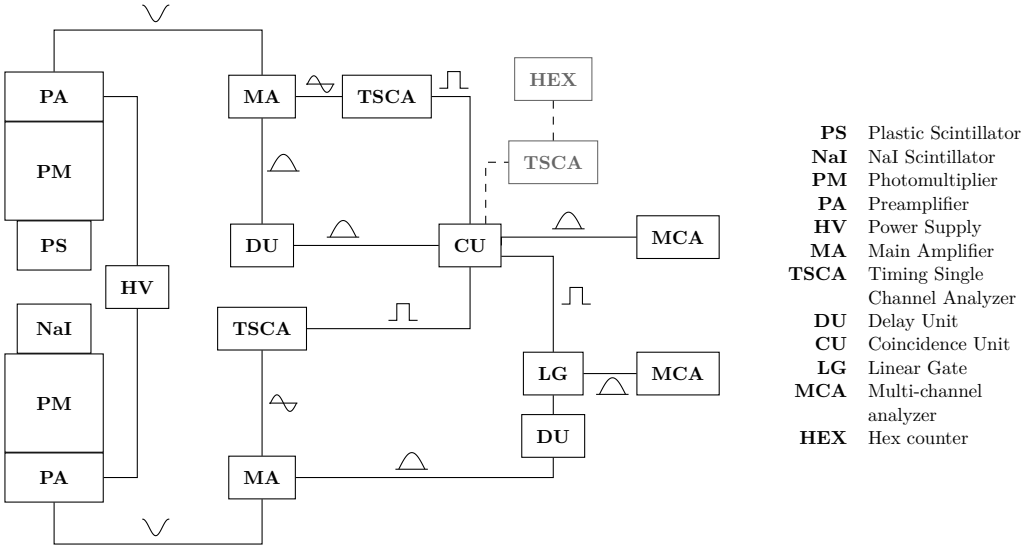

Figure 6: Plugging diagram of the NIM electronics of the experiment.

and we unnecessarily lose energy resolution and too high an amplification and we miss events that have a higher pulse height than the rightmost MCA channel. As we first did a very rough signal check using the oscilloscope to observe the shape of the signals, the amplification levels of our preliminary analysis differ from the main settings used for all measurements (cf. table 1).

Next, we set the delays on the TSCAs such that the logical signals arrive at exactly the right time when a highly correlated event is measured by both scintillators. This was done by connecting an oscilloscope to the logical output of both TSCAs and use one of the signals for triggering. Now, by adjusting the delay knobs on the TSCAs, the number of simultaneously observed signals could be maximized by hand. For the NaI TSCA we decided on a delay of 1.2 µs (delay knob on 0.2 setting with the delay switch on the 1.0–11 µs range) and for the plastic scintillator's TSCA we used a delay of 1.5 µs (delay knob on 0.5 setting with the delay switch set to the 1.0–11 µs range).

Further, the delay of the main (unipolar) signal from the main amplifiers (that later feed into the MCAs) had to be adjusted. This time we had to optimize for the maximum number of events within the coincidence time window set by the logical input signals of the TSCAs at the coincidence unit. By connecting the Hex counter as shown in gray in fig. 6 we were able to maximize the delay settings at the delay unit such that the number of signals recorded by the Hex counter within 10 s was maximal We fixed the delay for the NaI scintillator to be 3 µs and 4 µs for the plastic scintillator. With the final settings, using the ^{22}Na source, the Hex counter counted about 400 events in 10 s while it counted just about 20 events in the same time if the delay of the TSCA's was changed by a magnitude. So with this setting we yield a proportion of around 5% random coincidences.

Now that the delays were all set, it was important that none of the cables of the setup

were replaced or otherwise compromised as the delay settings we chose are specific to that cable configuration: By interchanging a cable for one with a higher or lower specific internal delay (due to e. g. material-specific signal loss), the delay settings specifically geared to the coincidence measurement could be thrown off.

After completing the setup we proceeded to record spectrums of both sources for both scintillators that are used for the energy calibration. By toggling a switch on the coincidence unit, a signal source could be disabled such that the full (i. e. coincidence-free) spectrum of the other scintillator could be registered in its respective MCA. Note that for measuring the ^{137}Cs spectrum with the NaI scintillator, the plastic scintillator was removed from the setup. For the NaI scintillator the spectra were measured for about $\approx 1\,\mathrm{h} - 2\,\mathrm{h}$ while the measurements of the spectra with the plastic scintillator were done as overnight measurement for the ^{137}Cs spectrum and was measured over the weekend for the ^{22}Na spectrum. Also the background was measured with each scintillator as an overnight measurement, for this the ^{137}Cs source was turned around.

After the spectrum measurement, the energy windows of the NaI TSCA were adjusted to the coincidence measurements. For that, we enabled the switches at the coincidence unit again and recorded spectra for a range of angles with a measurement duration of $\approx 1\,\mathrm{h}$. After each spectrum measurement, the lower and upper window of the NaI scintillator was set to match the coincidence peak. The settings we chose for each angle is shown in table 2. Now that the TSCA's energy windows were set, we proceeded to measure coincidence spectra for about 3 h each. Two exception to this duration are the 45° measurement, which was done as an over night measurement and the second 0° measurement which was only run about 1 h. Further it should be noted that the first measurements for 0°, 30° and 120° were done with the window of the plastic TSCA fully opened. Since this lead to a high number of random coincidences for small angles, 0° and 30° were measured again with the lower level of the window for the plastic scintillator being set to 0.1 which was also the case for all of the other measurements.

To be able to calculate the cross section correctly from the measurements, a measurement of the ^{137}Cs spectrum with the NaI scintillator through the plastic scintillator was done and also a random coincidence measurement, delay changed by about a magnitude, with the scattering angle set to 0° was done. Both measurements run about 1 h.

Table 1: Amplification levels of the main amplifiers.

	Preliminary analysis		Main settings	
Scintillator	Gain	Coarse gain	Gain	Coarse gain
NaI	4.0	100	5.0	100
Plastic	4.0	200	6.0	500

Table 2: Settings of the NaI TSCA along with the peak center's position (Channel) and the peak's width (Width).

Angle [°]	Lower window	Upper window	Channel	Width
−30	2.2	4.9	1250	600
0	3.0	6.5	1490	420
30	2.2	4.7	1270	500
45	2.0	4.5	1060	500
60	1.9	4.0	880	350
90	1.2	2.9	590	350
120	0.9	2.0	430	240

4. Analysis

4.1. Energy calibration

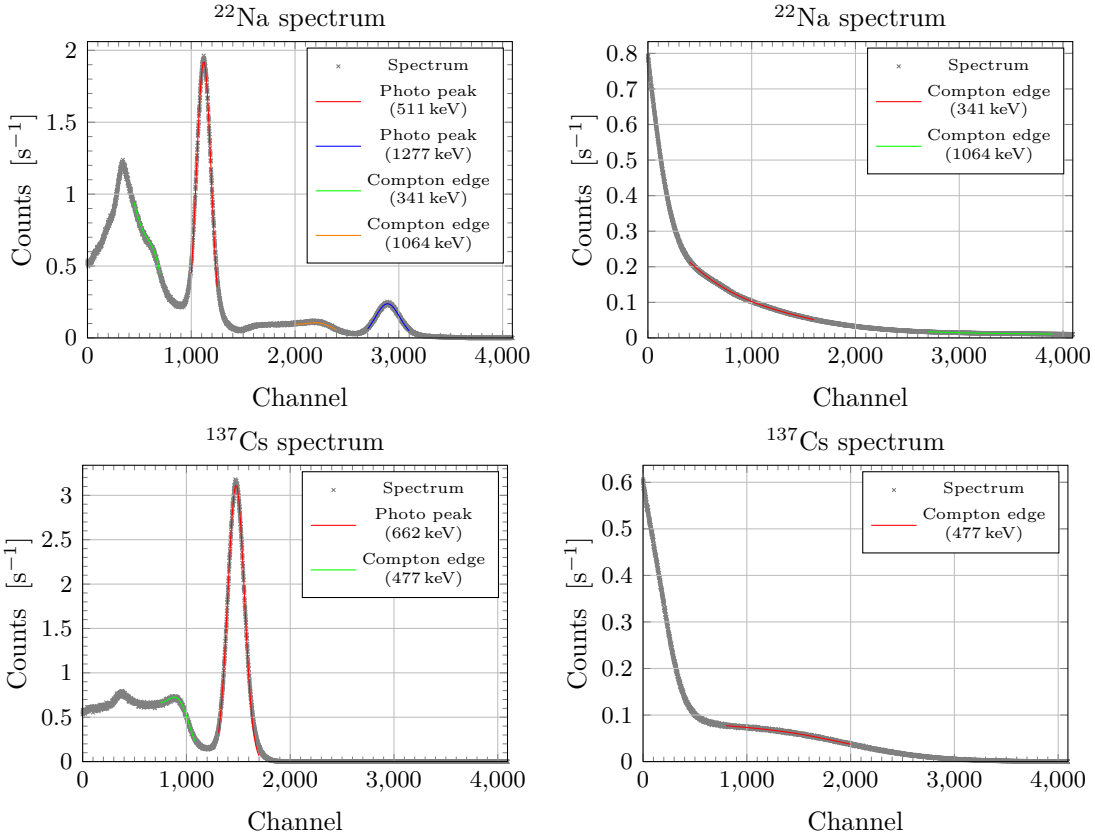

Figure 7: The spectra with subtracted background and the respective fits for the photopeaks and the Compton edges. The upper left shows the ^{22}Na spectrum measured with the NaI scintillator, the upper right the same spectrum measured with the plastic scintillator and the bottom pictures show the ^{137}Cs spectrum on the left measured with the NaI scintillator and on the right measured with the plastic scintillator.

To be able to assign energies to the channels of the MCA we first need to do an energy calibration. For this, the measured spectra of ^{137}Cs and ^{22}Na are used. Before the spectra were analyzed, the backgrounds measured for both scintillators was subtracted: to do so, the number of counts for each channel was divided by the duration of the respective measurement such that each measurement was expressed in counts per second. The spectra measured and the backgrounds can be found in the appendix (cf. figs. 17 and 18) and the spectra cleaned from the background can be seen in fig. 7. As is common practice, the uncertainty of the counts were estimated as Poisson error, i. e. the square root of the counts and were propagated using Gaussian error propagation.

Table 3: Fit parameter for the photopeaks measured with the NaI scintillator.

Peak		A [s^{-1}]	μ	σ	χ^2/df
^{22}Na	511 keV	1.923 ± 0.002	1120.23± 0.11	70.51± 0.17	14
^{22}Na	1277 keV	0.2374± 0.0005	2891.6 ± 0.3	117.7 ± 0.5	113
^{137}Cs	662 keV	3.120 ± 0.003	1478.88± 0.10	79.45± 0.13	19

Table 4: Two of the five fit parameters for the Compton edges measured with the two scintillators.

Scintillator	Compton Edge		Ch_C	σ	χ^2/df
NaI	^{22}Na	511 keV	670± 6	83± 4	1.7
	^{22}Na	1277 keV	2260± 30	152± 11	34
	^{137}Cs	662 keV	943± 10	104± 4	1.1
Plastic	^{22}Na	511 keV	710± 110	800± 40	0.2
	^{22}Na	1277 keV	3300± 1200	1300± 600	6
	^{137}Cs	662 keV	1400± 400	710± 110	6

For the Compton edges functions of the form eq. (14) were fitted against the data using the `curve_fit` method of the python module `scipy.optimize` [4] which is a non-linear least squares optimizer. The python method was supplied with the uncertainties of the counts which are used as weights in the fit. Gaussian functions of the form

$$F(x) = A \exp\left(-\frac{(x-\mu)^2}{2\sigma^2}\right) \tag{21}$$

were fitted to the data to determine the shape of the photopeaks, were A, μ and σ are the fit parameters. Again, the `curve_fit` method of the python module `scipy.optimize` was used for the fits and again the uncertainties of the counts were supplied.

The fits are shown in fig. 7 alongside the data used for the fit while the fit parameters that we received are given in table 3 for the photopeaks and the Compton edge parameter Ch_C and the parameter σ are given in table 4 while the other are to be found in the appendix in table 6. In addition, the residual standard error (written as χ^2/df) was calculated for each fit and can be found in the same tables as the fit parameter. The relatively high values for the photo peaks (especially the second ^{22}Na peak) are reasoned by a high fluctuation – at least in relation to the uncertainties – of the data at the top of the peaks. This however has not to much influence on the determination of the position of the peak in which we are mainly interested.

For the Gaussian fits the fit parameter μ represents the position of the photopeak while for the Compton edges the fit parameter Ch_C represents the position of the edge. The determined channels for this fit parameter were paired with the theoretical energies for the peaks and edges and a linear function of the form

$$Ch = \alpha \cdot E + \beta \tag{22}$$

was fitted to this data for each scintillator. The fits were again performed by `curve_fit` method of the python module `scipy.optimize` and for the channels the uncertainties given by the method were used. The data and the fits can be seen in fig. 8. For the fit parameters we got

$$\alpha_{\mathrm{NaI}} = (2.324 \pm 0.013)\,\mathrm{keV}^{-1}\,\mathrm{s}, \qquad \beta_{\mathrm{NaI}} = (-63 \pm 8)\,\mathrm{s}^{-1} \tag{23}$$

$$\alpha_{\mathrm{Plastic}} = (3.9 \pm 0.6)\,\mathrm{keV}^{-1}\,\mathrm{s}, \qquad \beta_{\mathrm{Plastic}} = (-600 \pm 200)\,\mathrm{s}^{-1}. \tag{24}$$

Again, we calculated the residual standard errors for the fits, the extraordinary high values for ^{22}Na calibration is reasoned by the small uncertainties of the photo peak positions, which have relative uncertainties of 0.01 % and smaller.

Now, the channels Ch now can be converted to energies with

$$E = \frac{Ch - \beta}{\alpha} \tag{25}$$

and the uncertainty of the energies can be calculated using the covariance matrix of the fit parameters and the uncertainty of the channel with

$$\sigma_E^2 = \begin{pmatrix} \frac{\partial E}{\partial Ch} & \frac{\partial E}{\partial \alpha} & \frac{\partial E}{\partial \beta} \end{pmatrix} \begin{pmatrix} \sigma_{Ch}^2 & 0 & 0 \\ 0 & \mathrm{cov}(\alpha,\alpha) & \mathrm{cov}(\alpha,\beta) \\ 0 & \mathrm{cov}(\beta,\alpha) & \mathrm{cov}(\beta,\beta) \end{pmatrix} \begin{pmatrix} \frac{\partial E}{\partial Ch} \\ \frac{\partial E}{\partial \alpha} \\ \frac{\partial E}{\partial \beta} \end{pmatrix} \tag{26}$$

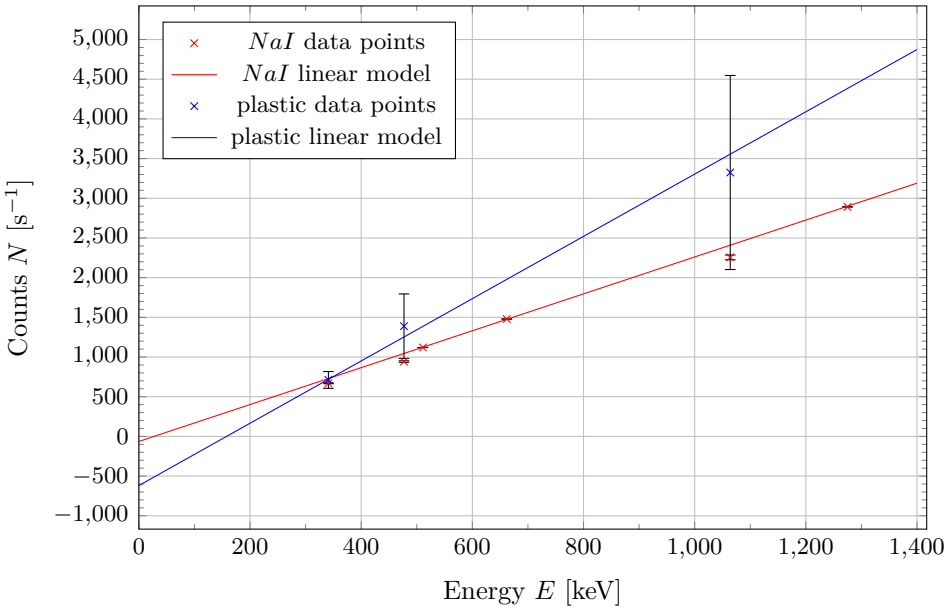

Figure 8: The energy calibration for each of the scintillator. For the NaI scintillator we calculated $\chi^2/\mathrm{df} = 995$ and for the plastic scintillator $\chi^2/\mathrm{df} = 0.2$.

Table 5: Photon and electron energies ($E_{\mathrm{NaI}}, E_{\mathrm{Plastic}}$) measured for the different angles and the according channels ($\mu_{\mathrm{NaI}}, \mu_{\mathrm{Plastic}}$) from which they were calculated. In addition the total energy calculated as sum of photon and electron energy.

Angle [°]	μ_{NaI}	E_{NaI} [keV]	μ_{Plastic}	E_{Plastic} [keV]	E_{total} [keV]
0	1503.7± 0.2	674 ± 2	–	–	–
0	1437 ± 4	645.5± 0.9	–	–	–
30	1248 ± 2	564.2± 1.4	−140± 60	80± 80	650± 80
30	1249.5± 1.6	565.0± 1.2	−120± 70	100± 80	660± 80
45	1084.9± 1.0	494.2± 1.3	157± 3	240± 20	730± 20
60	904.0± 1.8	416.3± 1.7	340± 4	331± 11	747± 11
90	594 ± 2	283 ± 2	459± 19	594± 2	742± 19
120	423.6± 1.9	209 ± 3	733± 6	530± 30	740± 30
−30	1199.4± 1.8	543.5± 1.3	−19± 15	150± 40	690± 40

4.2. Energy conservation

To check the energy conversation for the Compton scattering, we use the measurements for the different angles of the plastic and NaI scintillator in coincidence mode. Therefore, we first normalize the measured counts for each channel to counts per second by dividing them by the duration of that measurement. The uncertainty of the counts measured was again assumed to be the square root of the measured counts and propagate with Gaussian error propagation. Gaussian functions were fitted to each measurement in the same fashion it was done for the photopeaks in section 4.1. Plots of the measurements and the according fits can be found in the appendix (cf. figs. 13 to 16) as well as the resulting fit parameters (cf. tables 8 and 9).

Since the measurements with the plastic scintillator are quite noisy and the peaks relatively small we decided to re-bin the data, always merging two neighbouring channels starting at channel one. Using eq. (25) the means μ of the Gaussian fits were converted into energies and the errors propagated using eq. (26). Due to the fact that the energy calibration was done without re-binning the data, the obtained values for μ was doubled before using eq. (25) for the case of the measurement with the plastic scintillator. The obtained energies as well as the according means are to be found in table 5.

For each angle the sum of the energy measured in the plastic scintillator (the energy of the scattered electron) and the energy measured in the NaI scintillator (the energy of the scattered photon) was calculated which can also be found in table 5. The total energies as well as the one for the electron and photon are plotted against the scattering angle (cf. fig. 9). Also plotted as solid lines are the theoretically expected trends for the electron and photon energy in dependence of the scattering angle. It can be seen that although the total energy is not completely constant, the individual energies roughly follow the expected curves. The photon energy fits the expected course much better than that of the electrons, whose energies do not increase strongly enough with increasing angle to fit to the theoretical curve. As additional measure of the goodness of our data relative to the expected trend we also calculated the residual standard error for the photons and

electrons separately and for the total energy to be

$$\left(\chi^2/\mathrm{df}\right)_{\mathrm{photon}} = 94, \quad \left(\chi^2/\mathrm{df}\right)_{\mathrm{electron}} = 11, \quad \left(\chi^2/\mathrm{df}\right)_{\mathrm{total}} = 13. \tag{27}$$

While the residuals were calculated for the NaI and plastic scintillator with respect to the theoretical curves in fig. 9, the residuals for the total energy was calculated with respect to the sample mean of those data points. The high value for the photons are due to the small relative uncertainties also visible in fig. 9.

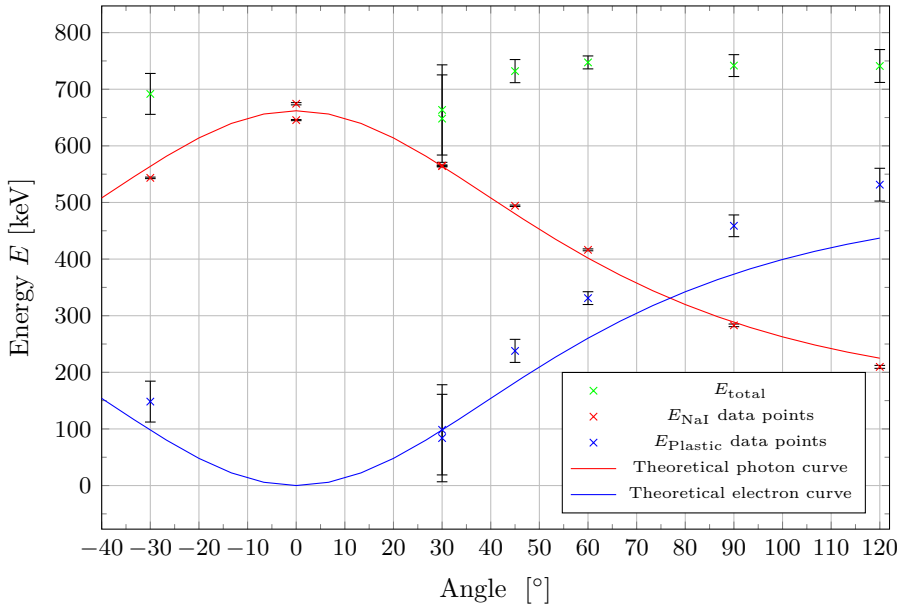

Figure 9: Plot of the measured energies of the scattered electrons and photons for different scatter angles and the total energy as well as the theoretical energy curves for the photons and electrons.

4.3. Cross section

For calculating the cross section the measurements for the different angles are used again but this time we just need the measurements of the NaI scintillator. To do so we calculate the total counts per second for each measurement by summing the counts over all channels and dividing by the total time of the measurement. Since the windows for some of the measurements were set a bit to wide we cut away some channels manually so only the peaks are considered. These cuts are marked in fig. 13 and fig. 14 in the appendix.

To calculate the cross section accurately, the measured count rates need to be corrected, which was done in the following way:

$$N_{\mathrm{corr}} = \frac{\eta \cdot 0.95}{\epsilon(E)\epsilon_{\mathrm{peak}}(E)} \exp\left\{\left(\mu(E) + \mu(622\,\mathrm{keV})\right)\frac{d}{2}\right\} \cdot N_{\mathrm{meas}}, \tag{28}$$

where $\epsilon(E)$ is the energy dependent efficiency to detect a photon of the NaI scintillator given by reference [5], ϵ_{peak} is the energy dependent intrinsic peak efficiency given in the same reference, μ (not to be confused by the fit parameter used earlier) is the energy dependent absorption coefficient of the plastic scintillator given in the instructions [6], $d = 1 \times 10^{-2}\,\text{m}$ the thickness of the plastic scintillator (in the case of the 90° measurement this thickness was corrected by dividing through $\cos(30°)$ since the plastic scintillator was rotated and therefore the effective thickness changed), the factor 0.95 takes the random coincidences into account which were measured with the ^{22}Na source to be about 5 % and η being the ratio between the ^{137}Cs photopeak measured with the NaI scintillator without and with the plastic scintillator between the source and the NaI scintillator. Both peaks used for the calculation of η are plotted in fig. 19 for comparison. The ratio itself was calculated by fitting Gaussian function – as done in section 4.1 – to both peaks and dividing the areas under both fits through each other. The ratio we calculated is $\eta = 1.07$. The values used for ϵ, ϵ_{peak} and μ for each measurement can be found in table 7. We decided to use the measurement with the ^{22}Na source instead of the measurement with the ^{137}Cs source, which was done under an angle of 0°, since it showed a proportion of random coincidences of about 30 %. A short analysis of the random coincidences with the Hex counter showed that the number of random coincidences drops massively with an increasing scattering angle, therefore a 30 % random coincidences correction would be much to high for every measurement, expect for the 0° measurement. Therefore we decided to use the 5 % measured with the ^{22}Na since it seems more reasonable for the other angles and we do not have measurements for each angle respective.

For the total count rate the rate measured for the ^{137}Cs spectrum with the NaI scintillator in section 4.1 was used. As for the count rates above the total count rate was calculated by summing over all channels contributing to the peak and it was than corrected by dividing it by the NaI scintillator efficiency $\epsilon(662\,\text{keV})$ and photopeak efficiency $\epsilon_{\text{peak}}(662\,\text{keV})$. This corrected total count rate is $N_{\text{total, corr}} = (1396.7 \pm 0.5)\,\text{s}^{-1}$.

Taking into account all these factors, the cross section for each angle was calculated as

$$\frac{\mathrm{d}\sigma}{\mathrm{d}\Omega} = \frac{1}{nd\Delta\Omega}\frac{N_{\text{corr}}}{N_{\text{total, corr}}}, \tag{29}$$

where $n = 3.4 \times 10^{23}\,\text{cm}^{-3}$ is the electron density of the plastic scintillator and $d = 1\,\text{cm}$ is its thickness, which is corrected for the 90° measurement as before and $\Delta\Omega = \frac{\pi r^2}{D}$ is the solid angle section over which we measure, $r = 3.81\,\text{cm}$ is the radius of the NaI scintillator and $D = (12.0 \pm 0.5)\,\text{cm}$ the distance between the two scintillators. These cross sections are plotted in fig. 10 as well as the cross section calculated with the Klein-Nishina formula as seen in eq. (15). The result for the measurement at 0° with fully opened TSCA is not plotted since it is more than two orders of magnitude larger as the other values, so no nice presentation would be possible. In order to be able to assess how well the data fits the Klein-Nishina formula we calculated the residual standard error to be $\chi^2/\text{df} = 7.4$ if one takes all of the measurements into account and $\chi^2/\text{df} = 1.2$ if one ignores the measurements for 0° since there are systematic problems with the measurement of the count rates for this angle setitng.

To be able to check if the deviation of our calculated values from the Klein-Nishina curve are mostly a wrong scaling we also normalized our results by dividing them by the measurement at 90° and doing the same with the Klein-Nishina formula (fig. 11). Also, in order to additional check the quality of the energies we determined in section 4.2, they were used in eq. (16) to calculate the cross section and were compared with the theoretical Klein-Nishina curve, to be seen in fig. 12.

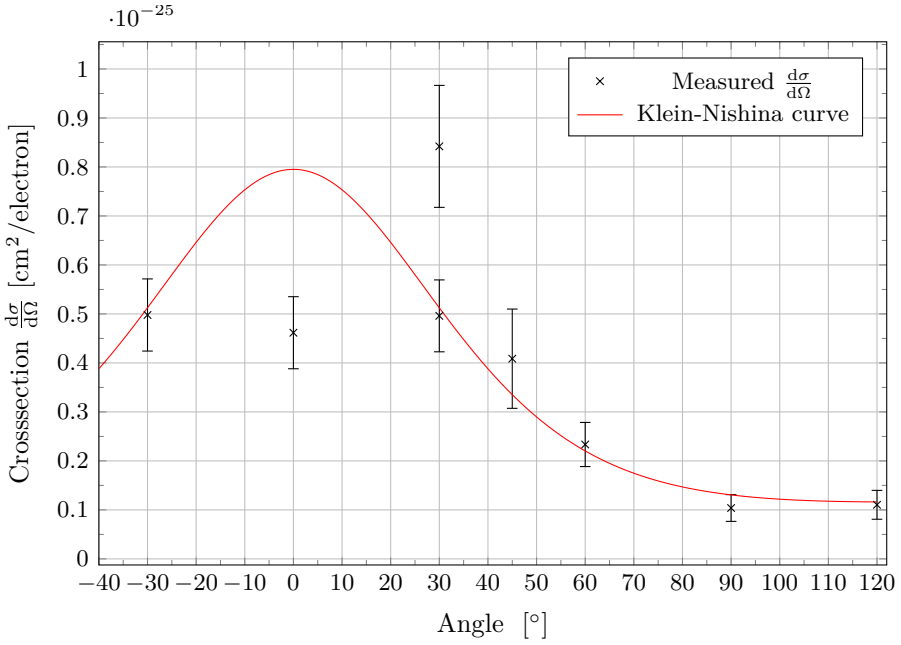

Figure 10: The calculated cross sections and the curve of the Klein-Nishina formula as solid line.

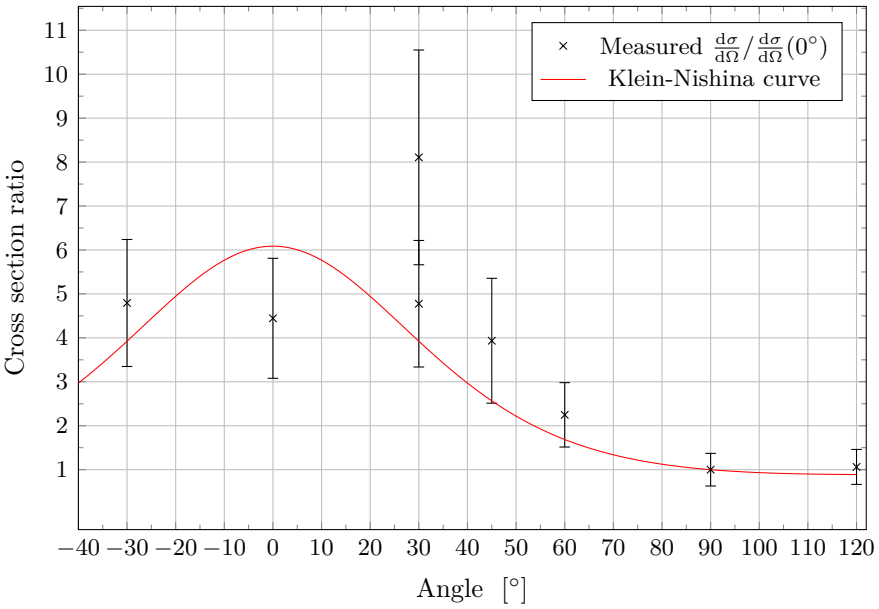

Figure 11: The calculated cross sections normalized by the value for 90° and the curve of the Klein-Nishina formula also normalized by its value at 90 degree as solid line.

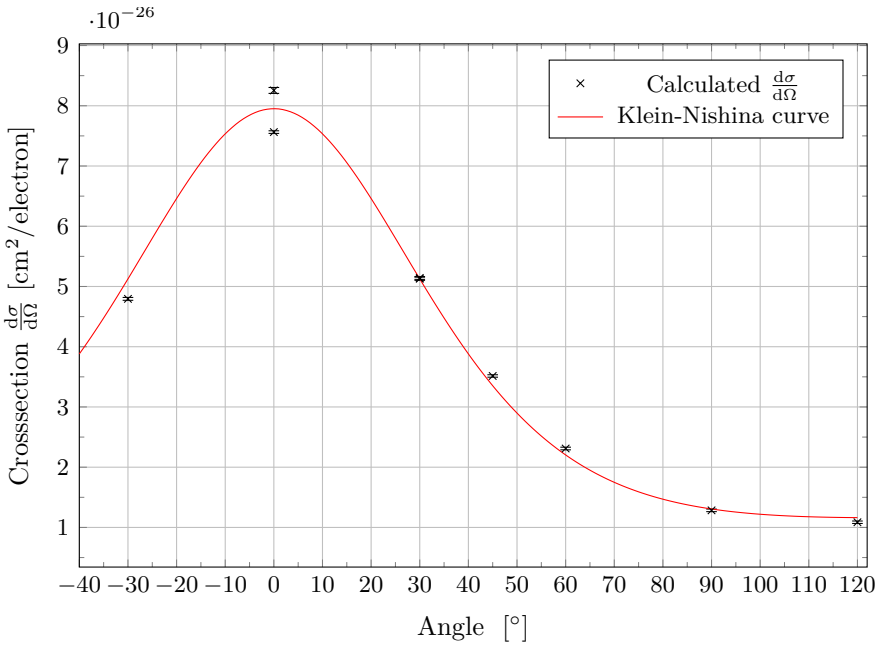

Figure 12: The cross section calculated with the energies determined for each angle in the measurements (cf. eq. (16)) and the curve of the Klein-Nishina formula as solid line.

5. Discussion

In the experiment we used the measurement of photons produced by a ^{137}Cs source with tow different scintillators in coincidence mode to study the energy conservation and the cross section for Compton scattering.

To do so, an energy calibration for both scintillator was performed which also worked in principle; however – especially for the plastic scintillator – the chance for systematic errors is quite high: One reason for this is that only three data points are provided for the linear model fit used for the energy calibration which is not much relative to the number of parameters in the linear model. For the NaI scintillator calibration, six data points are provided, which – statistically speaking – is also not to much, but still twice as many data points as for the plastic scintillator. This problem could be tackled by using different sources for the calibration. While this would result in less time available for the actual measurements (which is a problem we will talk about in subsequent paragraphs), but would help to gain a more reliable calibration.

The second difficulty for the calibration of the plastic scintillator is that the Compton edges used for the calibration are extremely blurred and difficult to see. To some degree, this is reasoned by the fact that plastic scintillators do not have the best energy resolution. However, the Compton edges measured with the experiment are said to have been much nicer a few years ago, which suggests that the blurring of the edges is at least partly a result from aging deficiencies of the scintillator.

Nevertheless, the calibration could be used to calculate the positions of the peaks, measured for different angles, into energies. The results of this calculations can be seen in fig. 9. The total energy differs over all $\propto 150\,\mathrm{keV}$. Although the total energy is by no means constant, the individual measurements for the scattered photons and electrons nevertheless follow the expected trends. The measured photon energies fit quite nicely to the expected curve, not differing too much. The energies of the electrons are much higher as the expectation, but this mostly looks like a global offset, since the trend itself seems pretty similar to the expected one. This offset, as mentioned above, could easily come from an systematic error in the energy calibration. If one does look at the residual standard error for the photons (cf. eq. (27)) one may be surprised by the high value, since optically the photon measurement fits better to the theoretical curve does as the electron one, but these high value probably come from the much smaller relative uncertainties for the fit parameters of the energy calibration as well as the once for the fit parameters determining the respective channel for the peak center. Thus, these uncertainties given by the used fit method seem to be a bit to small.

Furthermore, if considering the two different measurements for 30° it can be seen that the energies measured are quite compatible which indicates that there was no shift in the energy channel conversion of the MCA over the days the experiment was carried out. If one looks at the energy measured for $-30°$, the result does still roughly match with the other measurements but does show some shift to the 30° measurements. This could indicate that the angle settings at the experiment are a little bit off, with the results leading to the assumption that the 0° position marked at the experiment actually being some small negative angle. The two different measurements at 0° do differ a bit more.

This may could come due to the short run time for the second measurement. To further check the accuracy of the energy determination for the photons, we did calculate the cross sections for the different angles using the energies determined in the experiment which can be seen in fig. 12. It can be seen that the calculated cross sections follow the Klein-Nishina curve nicely and narrow.

The second point to study was the cross section of the Compton scattering. The results of this analysis can be seen in fig. 10 which roughly shows the expected trend of the Klein-Nishina curve but does differ quiet a bit. There are couple of possible explanations for this. One being the different corrections needed to calculate the actual cross section: For example, the absorption coefficient is just given for certain energies and the efficiencies are extracted from curves which are generated for similar systems as ours but don't match ours exactly which provides uncertainties which are difficult to estimate. However, the correction with the strongest influence for our calculations probably is the correction of random coincidences. The proportion of random coincidences is strongly angle dependent, being large for small angles and very low in comparison for larger angles. So, in order to more accurately take this factor into account, one option would be to measure the random coincidences for each angle individually and than subtract this random coincidence background from each measurement separately. To carry out those measurements with a satisfactory duration, however, would exceed the available time frame for this experiment.

A second source of uncertainty for the cross section measurements is the activity of the source. Since the event rates for some angles are rather small, one could argue that a measurement duration of 3 h is not long enough to average out variations in activity. This factor could be prevented by doing longer measurements (for which we again did not have the time).

If one compares the cross sections fig. 10 and the normalized cross sections fig. 11, one can see that the normalization had no real influence on the trend of the data. Therefore, one can argue that the deviations of the measurements from the Klein-Nishina formula do not come from any overall factor missing in the calculations but either due to energy/angle dependent corrections being not considered correctly (as for example the random coincidences) or due to fluctuations in the activity of the source as mentioned above.

Furthermore, if one looks at the three measurements which were done with fully open TSCA windows for the plastic scintillator, one can see that this had a great influence for the small angles with the 0° measurement exceeding the expected values by two orders of magnitude and the measurement at 30° not being as big, but still significantly greater as the other measurement for the same angle, while the measurement at 120° is in agreement with the expected value, even being a little bit to small. This observation agrees with the observation that the random coincidences depend strongly on the angle with a great variation especially for small angles.

Nevertheless, if one looks at the residual standard error (without taking into account the 0° measurements), which is $\chi^2/\mathrm{df} = 1.2$, one can say that our measurements agree with the Klein-Nishina formula. That we do not take into account the 0° measurements can be reasoned by the fact that, assuming the setup work perfectly, we should measure

no events for this angle, since the electrons should have zero energy and therefore not be detectable by the plastic scintillator. However, since the detectors do have a spatial coverage and other disturbing factors we do measure events. So the measurements at 0° are usable for the energy determination since the peak position is not affected by this facts, but is not reliable for the determination of the cross section.

Overall, one can say that for the energy conservation and the cross section, the theoretical trends can be seen in our measurements with some deviations for which possible reasons can be provided. Furthermore, the analysis shows that the energy determination with the experimental setup used works quite satisfactorily, especially in the case of the NaI scintillator – as expected. However, our analysis also shows that the determination of variables as the cross section which explicitly depend on the event rates are affected a lot more by experimental limitations and difficulties in, say, the extraction of the photopeak efficiency which lessens the overall accuracy for such variables.

List of Figures

List of Tables

References

[1] M.-M. Bé et al. *Table of Radionuclides*. Vol. 3. Monographie BIPM-5. Bureau International des Poids et Mesures, 2006. URL: http://www.bipm.org/utils/common/pdf/monographieRI/Monographie_BIPM-5_Tables_Vol3.pdf.

[2] M.-M. Bé et al. *Table of Radionuclides*. Vol. 5. Monographie BIPM-5. Bureau International des Poids et Mesures, 2010. URL: http://www.bipm.org/utils/common/pdf/monographieRI/Monographie_BIPM-5_Tables_Vol5.pdf.

[3] Arthur H. Compton. "A Quantum Theory of the Scattering of X-rays by Light Elements." *Phys. Rev.* 21 (5 1923), pp. 483–502. DOI: 10.1103/PhysRev.21.483.

[4] Jones; Eric, Travis Oliphant, Pearu Peterson, et al. *SciPy: Open source scientific tools for Python*. Online; Accessed on Aril 2nd, 2021. 2001–. URL: https://www.scipy.org/.

[5] S. Flügge and E. Creutz. *Instrumentelle Hilfsmittel der Kernphysik II*. Vol. XLV. Handbuch der Physik. 1958.

[6] M. Köhli. *Compton-Effekt. Fortgeschrittenen Praktikum II*. 2011.

[7] Hermann Kolanoski and Norbert Wermes. *Particle Detectors: Fundamentals and Applications*. Oxford University Press, 2020.

[8] S. A. *Properties of Nuclear Radiation*. Accompanying the experiment.

[9] M. H. Safari, F. A. Davani, and H. Afarideh. *Differentiation method for localization of Compton edge in organic scintillation detectors*. 2016. arXiv: 1610.09185 [physics.ins-det].

A. Appendix

Table 6: Three of the five fit parameter for the Compton edges measured with the two scintillator.

Scintillator	Compton Edge		a [10^{-8}]	b [10^{-3}]	c
NaI	^{22}Na	511 keV	580 ±30	−8.3 ± 0.4	3.45 ± 0.12
	^{22}Na	1277 keV	24 ± 8	−1.1 ± 0.5	1.3 ± 0.6
	^{137}Cs	662 keV	420 ±70	−6.9 ± 1.4	3.4 ± 0.7
Plastic	^{22}Na	511 keV	10.6± 0.6	−0.381± 0.017	0.342 ± 0.015
	^{22}Na	1277 keV	0.5± 0.4	−0.05 ± 0.04	0.09 ± 0.04
	^{137}Cs	662 keV	2.2± 1.9	−0.04 ± 0.03	0.089 ± 0.003

Table 7: Used efficiencies and coefficients for the correction of the counted rate, depending on the energy measured at the respective angle.

Angle [°]	E_{NaI} [keV]	ϵ	μ [cm^{-1}]	ϵ_{peak}
0	674 ± 2	0.42± 0.05	0.089	0.16± 0.01
0	645.5± 0.9	0.42± 0.05	0.089	0.16± 0.01
30	564.2± 1.4	0.45± 0.05	0.091	0.20± 0.01
30	565.0± 1.2	0.45± 0.05	0.091	0.20± 0.01
45	494.2± 1.3	0.48± 0.05	0.098	0.24± 0.05
60	416.3± 1.7	0.54± 0.05	0.108	0.34± 0.05
90	283 ± 2	0.7 ± 0.1	0.12	0.5 ± 0.1
120	209 ± 3	0.8 ± 0.1	0.136	0.9 ± 0.2
−30	543.5± 1.3	0.45± 0.05	0.098	0.20± 0.01

Table 8: The fit parameter for the peaks measured for different angles with the NaI scintillator.

Angle [°]	A_{NaI} [s^{-1}]	μ_{NaI}	σ_{NaI}	χ^2/df
0	0.1882 ± 0.0005	1503.7± 0.2	82.7± 0.2	1.2
0	0.002 80± 0.000 10	1437 ± 4	90 ± 6	1.1
30	0.004 58± 0.000 06	1248 ± 2	165 ± 3	1.4
30	0.003 45± 0.000 05	1249.5± 1.6	119.6± 2.0	1.0
45	0.003 64± 0.000 02	1084.9± 1.0	131.1± 1.1	1.4
60	0.002 99± 0.000 05	904.0± 1.8	122.8± 1.8	1.5
90	0.004 96± 0.000 08	594 ± 2	97 ± 2	1.9
120	0.011 40± 0.000 16	423.6± 1.9	90 ± 4	1.2
−30	0.003 44± 0.000 05	1199.4± 1.8	118 ± 2	1.1

Table 9: The fit parameter for the peaks measured for different angles with the plastic scintillator.

Angle [°]	A_P [s^{-1}]	μ_P	σ_P	χ^2/df
30	0.0050 ± 0.0007	−140± 60	240± 30	0.9
30	0.0042 ± 0.0005	−120± 70	270± 40	1.2
45	0.002 450± 0.000 015	157± 3	232± 3	1.2
60	0.001 55 ± 0.000 02	340± 4	236± 5	1.1
90	0.001 217± 0.000 020	590± 5	288± 7	1.1
120	0.001 13 ± 0.000 02	733± 6	281± 9	1.3
−30	0.003 39 ± 0.000 10	−19± 16	227± 8	1.0

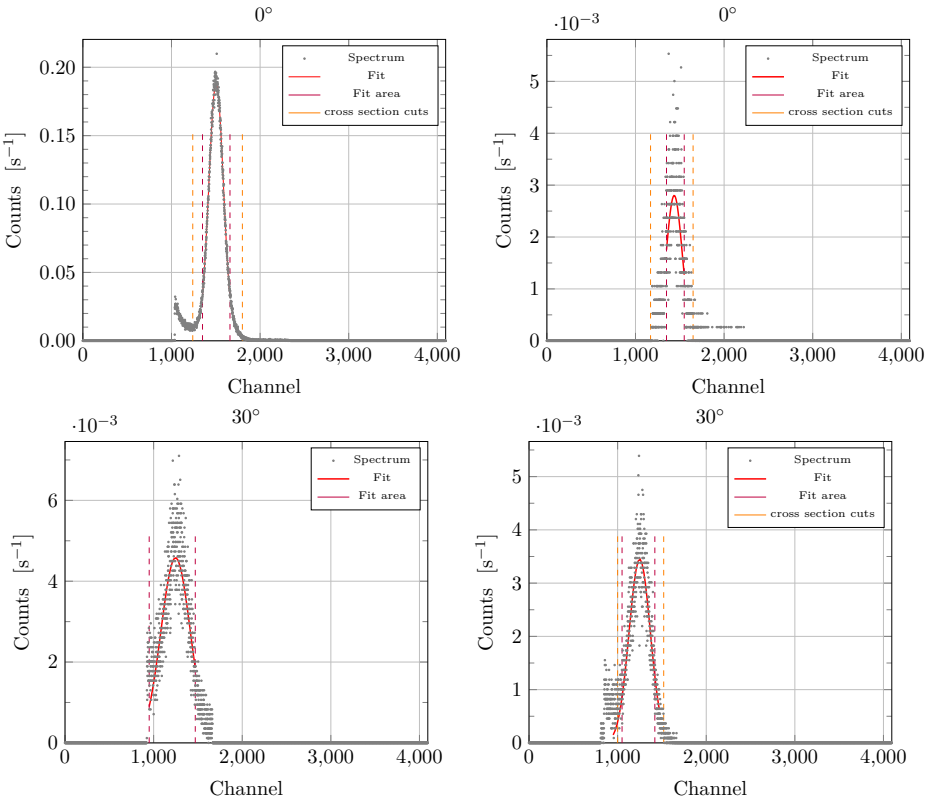

Figure 13: Measurements of the NaI scintillator for different angles, also shown are the fits used for the energy determination and the sections of the data which were used for the fits or the cross section calculations.

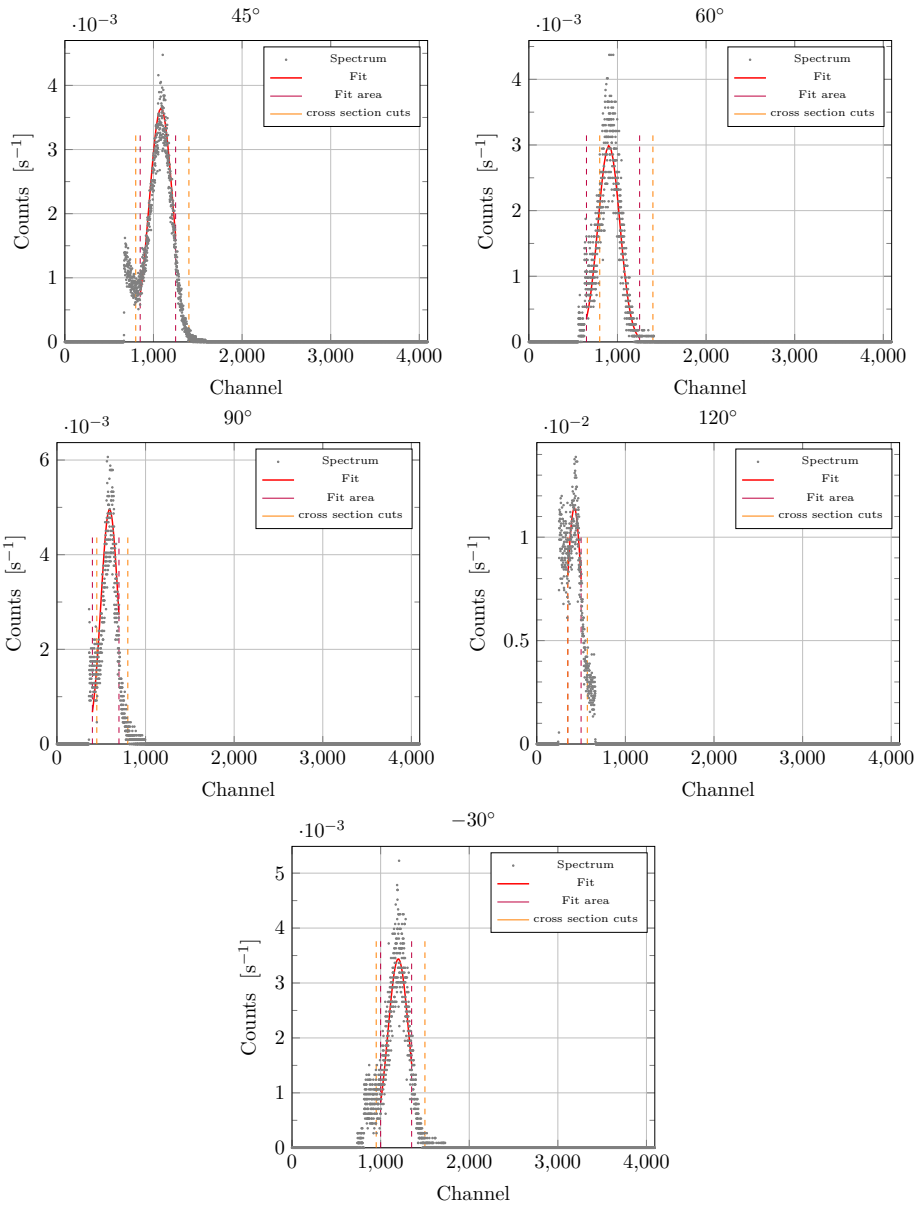

Figure 14: Measurements of the NaI scintillator for different angles, also shown are the fits used for the energy determination and the sections of the data which were used for the fits or the cross section calculations.

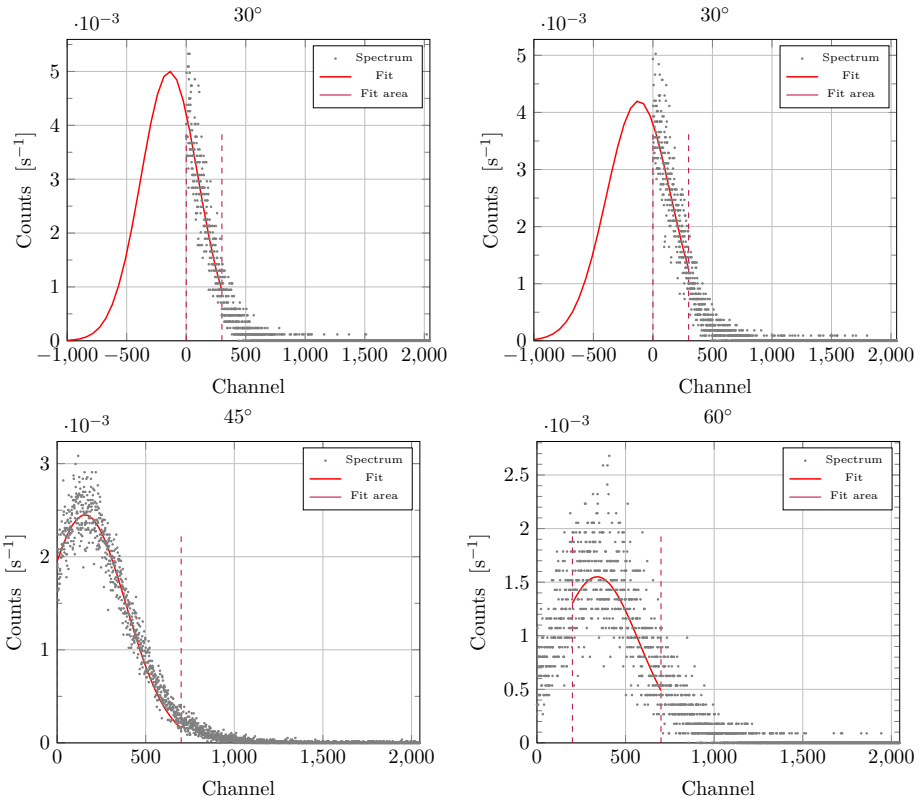

Figure 15: Measurements of the plastic scintillator for different angles, also shown are the fits used for the energy determination and the sections of the data which were used for the fits or the cross section calculations.

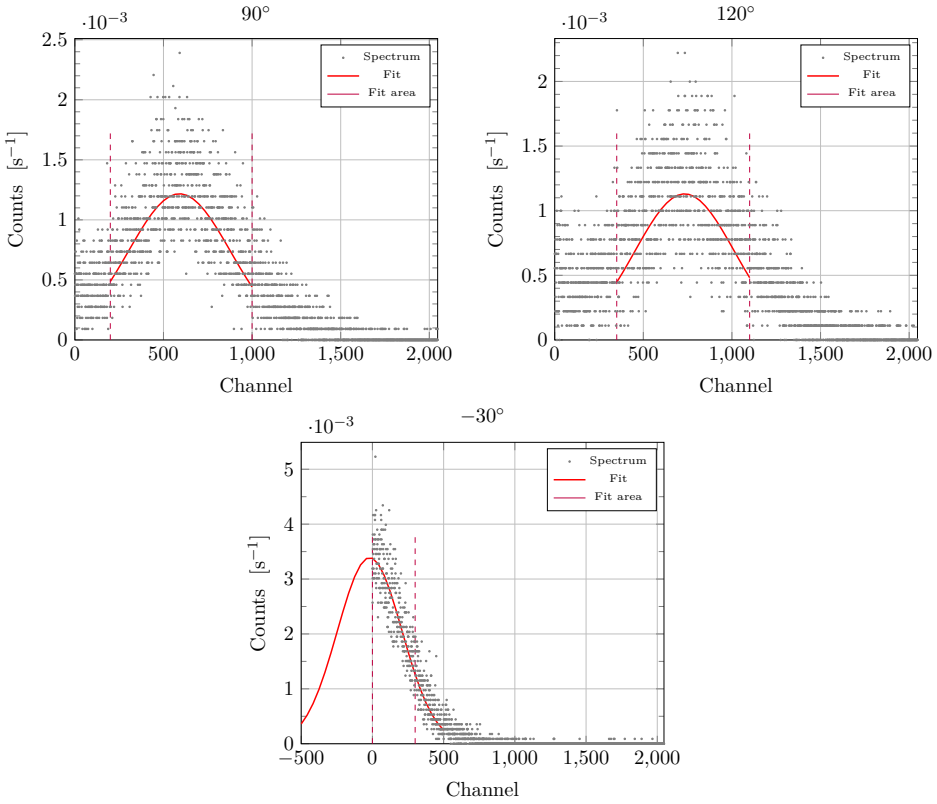

Figure 16: Measurements of the plastic scintillator for different angles, also shown are the fits used for the energy determination and the sections of the data which were used for the fits or the cross section calculations.

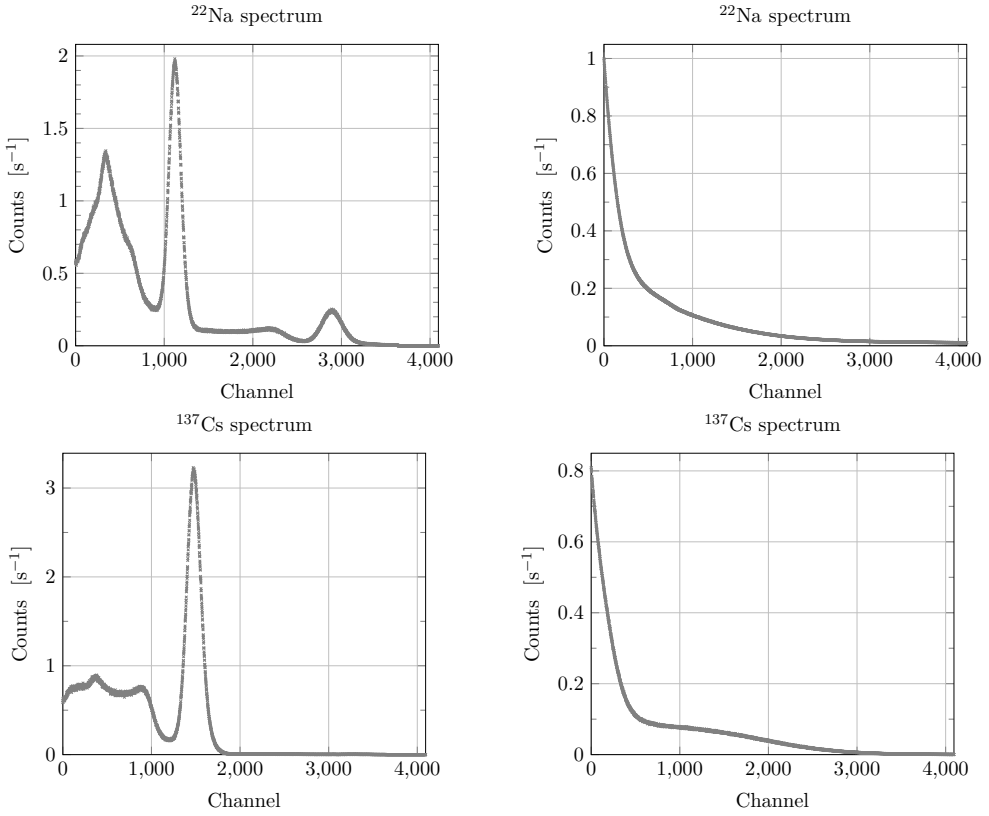

Figure 17: The spectra without subtracted background. The upper left shows the ^{22}Na spectrum measured with the NaI scintillator the upper right the same spectrum measured with the plastic scintillator and the bottom pictures show the ^{137}Cs spectrum on the left measured with the NaI scintillator and on the right measured with the plastic scintillator.

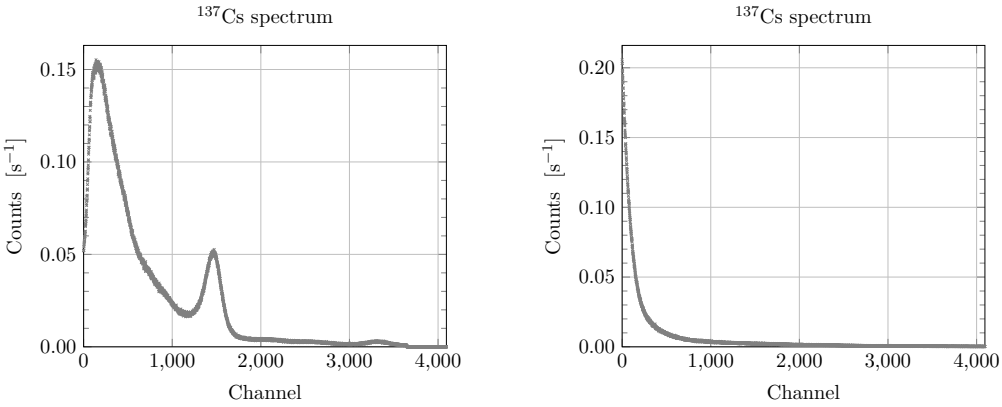

Figure 18: The background measured with both scintillator. On the left side for the NaI and on the right side for the plastic scintillator.

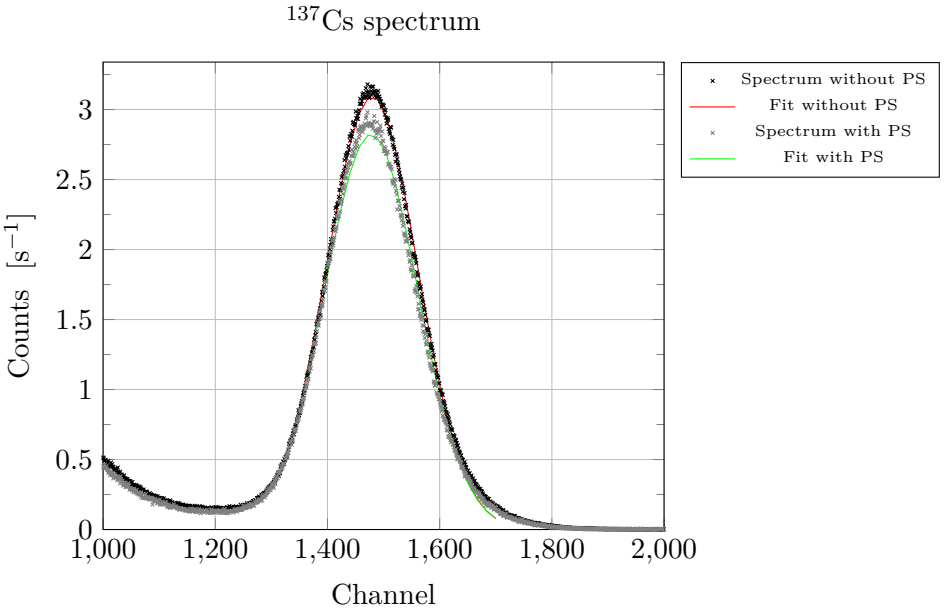

Figure 19: The ^{137}Cs photo peak measured with the NaI scintillator once measured without anything between the source and the scintillator (black) and once measured with the plastic scintillator standing in between (green).